Chemical Geology 351 (2013) 324–334

Contents lists available at SciVerse ScienceDirect

Chemical Geology

journal homepage: www.elsevier.com/locate/chemgeo

Zircon saturation re-revisited

Patrick Boehnke [a,*], E. Bruce Watson [b], Dustin Trail [b], T. Mark Harrison [a], Axel K. Schmitt [a]

[a] Department of Earth and Space Sciences, University of California, Los Angeles, CA 90077, United States
[b] Department of Earth and Environmental Sciences, Rensselaer Polytechnic Institute, Troy, NY 12180, United States

ARTICLE INFO

Article history:
Received 24 July 2012
Received in revised form 29 March 2013
Accepted 25 May 2013
Available online 1 June 2013

Editor: D.B. Dingwell

Keywords:
Zircon
Magma
Saturation
Zirconium

ABSTRACT

Improvements in experimental, analytical and computational methodologies together with published studies yielding seemingly contradictory results prompted us to return to the determination of zircon stability in the range of felsic to intermediate melts expected in continental environments. We (re-)analyzed both the run products from the zircon crystallization study of Watson and Harrison (1983) and a new style of zircon dissolution experiments (up to 25 kbar) using a large radius ion microprobe to constrain a refined zircon solubility model. The new data yield broadly similar patterns as before when arrayed for temperature and confirm that the parameter M [$=(\mathrm{Na}+\mathrm{K}+2\mathrm{Ca})/(\mathrm{Al}\cdot\mathrm{Si})$] is an appropriate compositional proxy for the chemical interactions through which zircon is dissolved. We used a Bayesian approach to optimize the calculation of the coefficients in the zircon solution model, which is given by:

$$\ln\ D_{\mathrm{Zr}} = (10108 \pm 32)/T(\mathrm{K}) - (1.16 \pm 0.15)(M-1) - (1.48 \pm 0.09)$$

where D_{Zr} is the distribution coefficient of Zr between zircon and melt and the errors are at one sigma. Sensitivity tests indicate that temperature and composition are the two dominant controls on zircon solubility in crustal melts with no observable effects due to pressure (up to 25 kbar) or variable water content. Comparison of the down-temperature extrapolation with natural examples confirms the validity of the model at ca. 700 °C.

1. Introduction

The recognition in the early 1980s that accessory minerals (e.g., zircon, monazite and apatite) are the principal hosts in the continents for geochemically important trace elements such as U, Th, and REE (Foucade and Allegre, 1981; Gromet and Silver, 1983; Harrison et al., 1986) inspired experimental studies into their stability in crustal melts (Harrison and Watson, 1983; Watson and Harrison, 1983; Harrison and Watson, 1984; Rapp and Watson, 1985).

Because of its near ubiquitous presence in continental rocks and key role as a U–Pb chronometer, the solubility of zircon in a variety of melt compositions was the first to be extensively investigated (Watson, 1979; Dickinson and Hess, 1982; Harrison and Watson, 1983; Watson and Harrison, 1983). Watson and Harrison (1983) undertook experiments in which zircon was crystallized from seed $\mathrm{ZrO_2}$ under hydrothermal conditions from mixtures of five glasses ranging from felsic to mafic in composition. Electron microprobe analysis (EPMA) of glass portions of the run products showed that zircon solubility in crustal magmas was a simple function of temperature, Zr content and composition. Notably, the parameter M [$=(\mathrm{Na}+\mathrm{K}+2\mathrm{Ca})/(\mathrm{Al}\cdot\mathrm{Si})$] was shown to be a good compositional proxy for the mechanism of zircon solution (note that M is calculated by obtaining the molar amounts of each component, renormalizing, and then obtaining the ratio). Their summary model for zircon solubility was given by

$$\ln D_{\mathrm{Zr}} = \frac{12900}{T(K)} - 0.85\cdot(M-1) - 3.80 \tag{1}$$

where $\ln D_{\mathrm{Zr}}$ is the distribution coefficient determined by ratioing the zirconium abundance [Zr] for zircon (i.e., [Zr] = 500,000 ppm) and melt (in ppm).

Harrison and Watson (1983) undertook zircon dissolution experiments that provided reversal confirmation of the crystallization studies, at least for the anhydrous case. It was found that zircon is relatively insoluble in anatectic melts. For example, a minimum melt at ca. 700 °C was found to dissolve only ~40 ppm zircon, corresponding to about one-fifth of the average Zr concentration in the crust (e.g., Rudnick and Gao, 2003).

The results of these experiments have been widely used to predict the occurrence of zircon in crustal magmas and to estimate the peak temperature experienced by magmatic rocks (i.e., accessory mineral thermometry; Watson and Harrison, 1984a,b). However limitations in both the analytical and experimental approaches restricted the resolution of the model. From the experimental perspective, many crystallization run products were complex mixtures of micron-sized crystals, glass and bubbles. This made electron microprobe analysis problematic as it was difficult to avoid overlapping the electron

---

[*] Corresponding author.
E-mail address: pboehnke@gmail.com (P. Boehnke).

0009-2541/$ – see front matter © 2013 Elsevier B.V. All rights reserved.
http://dx.doi.org/10.1016/j.chemgeo.2013.05.028

beam onto adjacent crystals and secondary fluorescence effects could contribute signal from adjacent nm-scale zircons undetected in micrographs. This can be seen in Fig. 1, a Zr ion image of one of the original run products showing abundant, tiny neoformed zircons (bright spots within the Zr-saturated glass). The above effects contributed to overall poor precisions for temperatures below ~900 °C (e.g., data at 750 °C could have ±100% uncertainty). Furthermore, subsequent published studies of zircon solubility in similar melt compositions yielded results that appeared somewhat at variance with that of Watson and Harrison (1983). Baker et al. (2002) found Zr dissolved at levels about one-third of that measured by Watson and Harrison (1983). They attributed this discrepancy to the higher f_{O_2} in their experiments which produced higher concentrations of Fe^{3+} which acted as a network former, thus reducing zircon solubility (and, effectively, *M*). Ellison and Hess (1986) examined Zr solubility in anhydrous melts at 1400 °C and 1 atm and found that the model of Watson and Harrison (1983) overpredicted their results by about 40%. Keppler (1993) examined the effect of halogens on granitic melt structure under similar conditions as that of Watson and Harrison (1983) and found similar Zr solubilities to theirs in halogen-free melts. However, solubility rose quasi-geometrically when ≥2% F was added. More recently, Rubatto and Hermann (2007) measured Zr solubility in peraluminous melts at 20 kbar and reported Zr concentrations ~40% lower than that of Watson and Harrison (1983) for the same temperature and composition. They attributed this difference to a previously undocumented pressure effect. Thus we have returned to this investigation 30 years later with a view to using an improved experimental design along with the superior sensitivity of a high resolution ion microprobe and improved computational methods to re-examine zircon solubility in crustal melts as a function of temperature, composition, and pressure.

2. Methods

2.1. Experimental approach

Most of the experiments reported by Watson and Harrison (1983) involved nucleation and growth of zircon from pre-synthesized ZrO_2-bearing glasses, followed by the measurement of Zr concentration in the quenched glass to determine the saturation level. This strategy was generally successful, but it also created analytical challenges because of the high nucleation density of zircon and its tendency to form small, needle-like crystals (Fig. 1). The 1983 study also included a few high-temperature reversal experiments in which large zircon slabs were partially dissolved in the melt. In this case, the Zr saturation level was estimated from the diffusion profile in the quenched glass near the dissolving zircon. The value of [Zr] at the zircon/glass interface – obtained by fitting the diffusion profile – was taken as the saturation concentration (see also Harrison and Watson, 1983). Although indirect, this approach offers the advantage of providing a clear field of quenched melt (free of small zircons) to analyze for Zr.

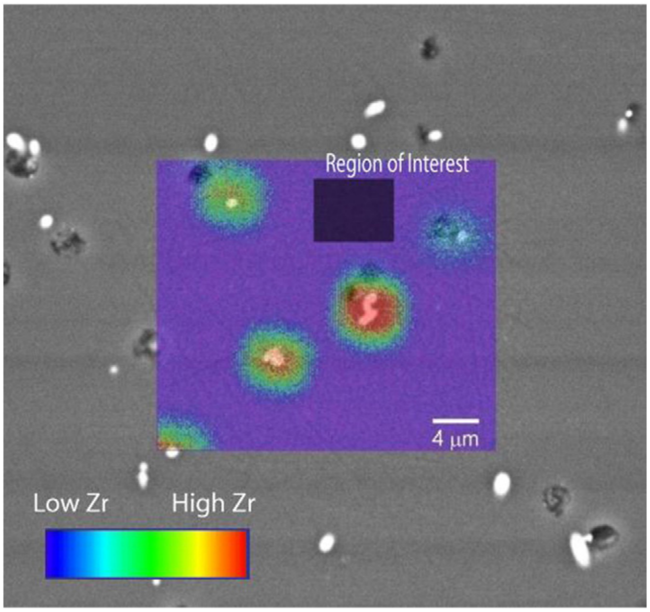

Fig. 1. Scanning ion image of a run product from Watson and Harrison (1983) superimposed on the BSE image. The bright areas are neoformed zircons whereas the shaded region is the area from which the saturation concentration is calculated ([Zr] = 367 ppm). The diffuse appearance of the ion-imaged zircon is not an effect of diffusion but rather due to the beam diameter (~3 μm).

In the 1983 studies, the partial dissolution method yielded good information at 1200–1400 °C but the prospects for obtaining data at temperatures approaching those relevant to natural systems were considered poor because Zr diffusion in silicic melts is slow (Harrison and Watson, 1983), and the resulting Zr profiles against a dissolving zircon slab would be too short for accurate characterization with available instruments. In the present study, we adopted a conceptually similar dissolution approach (to avoid the problem of myriad small crystals), but instead of immersing a large slab of zircon in the melt of interest, we equilibrated small, interstitial melt pools (10–20 μm dia.) with a surrounding matrix of crushed zircon.

2.2. Starting materials

In keeping with the general strategy used by Watson and Harrison (1983), five starting compositions were prepared to yield a range of crustal melt compositions when heated under pressure in the presence of zircon. The nominal bulk compositions range from mafic tonalite to rhyolite (Table 1; note that these do not represent actual melt compositions because crystalline phases in addition to zircon and glass were present in most run products; see Table 2). These five compositions were prepared from reagent-grade oxides and natural minerals, including $CaSiO_3$, Mg_2SiO_4, FeO, TiO_2, Al_2O_3, microcline and albite (all purchased from Alfa Aesar). These components were pre-mixed to yield compositions deficient in SiO_2 and Al_2O_3 so the latter oxides could be "topped up" as silicic acid and $Al(OH)_3$ to set the amount of H_2O contained in the mixtures (silicic acid contains 12.3 wt.% H_2O [quantified repeatedly by LOI]; gibbsite contains 34.6 wt.%). Introduction of H_2O in this manner made it possible to accurately regulate the bulk H_2O content of the non-zircon portion of the experimental charges at 5.9 ± 0.2 wt.%. The oxide/mineral mixtures were ground in agate under alcohol and dried at room temperature before use.

Additionally, four relatively mafic compositions were prepared in order to evaluate zircon solubility in such systems at near-liquidus temperatures under dry conditions. These consisted of a natural N-MORB, a synthetic tonalite, a synthetic high-alumina basalt, and a natural basaltic

Table 1
Anhydrous compositions of starting materials used in this study. These compositions were prepared by weighing $CaSiO_3$, Mg_2SiO_4, FeO, TiO_2, Al_2O_3, microcline, albite, silicic acid and $Al(OH)_3$ in appropriate portions to yield the rock-forming oxides shown plus 6 wt.% H_2O. See text for discussion.

Oxide	LCO	B	C	TN	BTC
SiO_2	77.0	73.7	70.2	61.9	65.8
TiO_2	0.1	0.3	0.5	0.8	0.8
Al_2O_3	13.1	13.5	13.9	16.9	18.6
FeO	0.7	1.8	2.9	5.8	4.8
MgO	0.1	1.1	2.2	3.0	1.6
CaO	0.5	1.7	3.1	5.7	2.8
Na_2O	3.7	3.6	3.5	3.9	1.7
K_2O	4.8	4.3	3.7	2.0	3.8
Total	100.0	100.0	100.0	100.0	99.9

Table 2
Summary of phases additional to zircon present in the experimental run products.

Sample	Phases present
ZSAT5A	Quartz
ZSAT7A	None
ZSAT7B	Pyroxene
ZSAT7C	Pyroxene
ZSAT7D	Amphibole, feldspar
ZSAT7E	Garnet, corundum
ZSAT9A	Quartz, feldspar, kyanite, garnet
ZSAT9B	Quartz, pyroxene, garnet
ZSAT9C	Quartz, garnet, pyroxene, rutile
ZSAT9D	Amphibole, garnet
ZSAT9E	Quartz, garnet, kyanite, rutile
ZSAT10A	Quartz, garnet, kyanite
ZSAT10B	Quartz, pyroxene, garnet
ZSAT10C	Quartz, pyroxene, garnet
ZSAT10D	Pyroxene, garnet
ZSAT10E	Quartz, garnet, kyanite, rutile
ZSAT11B	None
ZSAT11C	None
ZSAT11D	None

andesite from Paricutin volcano. The natural materials were run as finely-ground rock powders; the two synthetic mixes were fused and quenched to glasses prior to running the zircon saturation experiments in a piston-cylinder apparatus. Because these compositions strongly deviate from all of our other experiments, they are excluded from the zircon saturation calibration but discussed separately later.

A key aspect of this study involved the calibration of matrix effects on sample sputtering during SIMS analysis for Zr (see SIMS analytical details section). Sputtering behavior is expected to depend not only upon major-element composition of the analyzed glasses, but also upon the presence and amount of dissolved H_2O. We prepared three reference glasses and mixed them with USGS standard AGV-1 (236 ppm Zr) and Lake County obsidian (138 ppm Zr) in various proportions to create a broad composition range (e.g., Table 3). These materials were fused in a piston-cylinder apparatus both anhydrous (in graphite) and hydrous (in graphite encased in Ni) to obtain glasses suitable for electron- and ion-microprobe analysis.

3. Experimental procedures

The zircon saturation experiments were conducted in a piston-cylinder apparatus using two container designs. The high-temperature series (ZSAT11; 1020 °C) required gold capsules; all other experiments were conducted in silver cylinders incorporating a separate chamber (or “well”) for each of the five starting compositions described above (Table 1), plus a central buffer chamber to control the oxygen fugacity of the samples (see Fig. 2a). Prior to an experiment, each of the sample chambers of the silver cylinder was filled to 1/2 to 2/3 its full height with one of the five synthetic rock mixes. The remaining space at the top was filled with either crushed Mud Tank zircon or a mixture of

Table 3
Complete experimental results including run duration (hours), *T* (°C), *P* (kbar), major oxide composition of the melt (wt.%), and [Zr] (ppm).

Sample	Duration	*T*	*P*	Analytical total	SiO_2	TiO_2	Al_2O_3	FeO	MgO	CaO	Na_2O	K_2O	*M*	[Zr]	2σ
1	44	930	6.0	88.4	54.2	0.5	16.9	4.1	2.0	7.6	2.3	0.8	1.90	1442	117
2	44	930	6.0	88.9	56.2	0.6	16.8	3.1	1.6	5.9	3.3	1.4	1.79	1339	119
3	44	930	6.0	90.2	57.4	0.7	16.8	2.6	1.2	4.8	3.7	3.0	1.83	1405	121
4	44	930	6.0	88.9	58.8	0.6	17.1	3.6	1.4	2.6	1.5	3.3	1.01	367	47
5	19	1020	6.0	91.3	56.5	0.5	16.8	3.4	2.4	8.4	2.5	0.8	2.09	3178	332
6	19	1020	6.0	92.2	58.2	0.7	16.6	2.6	2.4	6.8	3.4	1.5	2.02	2801	285
7	19	1020	6.0	91.2	58.4	0.7	16.1	2.2	1.5	5.6	3.7	3.0	2.05	3452	342
8	19	1020	6.0	92.1	61.6	0.8	17.7	2.8	1.4	2.8	1.4	3.6	1.01	864	107
9	50	930	6.0	92.0	66.6	0.4	13.6	1.2	0.6	2.1	3.5	4.0	1.52	701	97
10	50	930	6.0	90.9	63.8	0.4	14.2	1.6	0.8	3.0	3.5	3.6	1.63	852	130
11	50	930	6.0	89.6	58.9	0.7	15.8	4.1	1.4	5.6	2.2	0.9	1.50	917	139
12	50	930	6.0	91.2	59.4	0.7	16.5	3.2	1.5	4.7	3.4	1.8	1.61	995	63
13	50	930	6.0	91.6	59.4	0.6	17.2	2.3	0.8	4.4	3.6	3.3	1.70	1183	98
14	50	930	6.0	95.1	64.2	0.6	17.8	3.7	1.6	1.8	1.6	3.8	0.88	300	75
15	284	800	1.7	91.2	68.1	0.1	13.0	1.1	0.1	1.2	3.4	4.2	1.36	155	14
16	284	800	1.7	91.7	68.1	0.2	13.0	1.0	0.1	1.2	3.6	4.5	1.44	223	59
20	284	800	1.7	92.3	69.5	0.2	13.2	1.4	0.7	1.5	1.6	4.2	1.05	226	65
21	240	800	1.2	92.5	66.6	0.2	13.7	1.4	b.d.	0.8	4.6	5.2	1.61	748	53
22	240	800	1.2	92.0	66.4	0.2	14.2	1.2	b.d.	1.4	3.8	4.8	1.47	452	29
24	240	800	1.2	92.4	68.5	0.4	13.3	1.9	0.8	1.6	1.7	4.2	1.10	178	24
25	240	750	2.1	91.2	68.9	0.1	12.4	0.9	b.d.	1.0	3.5	4.4	1.41	206	30
26	240	750	2.1	91.3	69.0	0.1	12.6	1.0	b.d.	1.0	3.0	4.6	1.32	265	50
ZSAT5A	72	850	10	92.4	71.9	0.1	12.2	0.7	0.1	0.2	3.6	3.5	1.15	277	15
ZSAT7A	48	925	10	92.6	71.7	0.1	12.1	0.8	0.1	0.2	4.1	3.5	1.24	666	35
ZSAT7B	48	925	10	93.6	70.4	0.2	12.4	1.3	0.7	1.3	4.1	3.3	1.46	742	40
ZSAT7C	48	925	10	93.9	68.3	0.4	13.2	1.9	0.9	2.0	4.2	3.0	1.55	849	56
ZSAT7D	48	925	10	93.4	64.1	0.4	15.0	3.0	0.9	3.3	4.3	2.3	1.63	1000	69
ZSAT7E	48	925	10	94.5	65.3	0.5	15.7	2.9	0.8	3.2	3.4	2.7	1.42	755	52
ZSAT9A	45	930	24[*]	94.2	68.3	0.8	15.2	0.8	0.1	0.3	4.9	4.6	1.34	968	92
ZSAT9B	45	930	24[*]	94.1	67.9	0.5	15.0	0.7	0.3	1.0	4.6	4.5	1.43	1084	82
ZSAT9C	45	930	24[*]	93.9	68.1	0.3	14.6	0.7	0.3	1.1	4.6	4.0	1.42	842	69
ZSAT9D	45	930	24[*]	92.9	66.7	0.3	15.6	0.7	0.3	2.0	5.0	2.4	1.39	749	61
ZSAT9E	45	930	24[*]	94.4	68.0	0.3	15.3	0.7	0.2	1.3	3.8	4.8	1.35	933	76
ZSAT10A	48	1000	25	95.2	70.4	0.1	13.9	0.9	0.2	0.3	5.0	4.3	1.42	1396	112
ZSAT10B	48	1000	25	95.5	69.3	0.2	14.6	0.3	0.9	1.0	4.9	4.3	1.49	1060	84
ZSAT10C	48	1000	25	95.4	69.1	0.4	14.7	0.9	0.4	1.4	4.7	3.7	1.45	1333	104
ZSAT10D	48	1000	25	93.5	65.9	0.5	15.8	1.1	0.4	2.5	5.1	2.1	1.49	1358	116
ZSAT10E	48	1000	25	94.4	68.1	0.4	14.8	0.9	0.2	1.7	3.7	4.5	1.42	2318	229
ZSAT11B	96	1020	10	95.4	71.0	0.2	13.6	0.4	1.0	1.7	4.3	3.2	1.45	996	38
ZSAT11C	96	1020	10	93.1	66.7	0.5	13.4	1.1	1.9	2.8	4.0	2.7	1.64	1692	39
ZSAT11D	96	1020	10	89.2	57.0	0.8	16.0	2.4	2.6	5.1	3.7	1.6	1.81	2384	67

[*] Pressure dropped from 25 to 23.5 kbar throughout the course of the run.

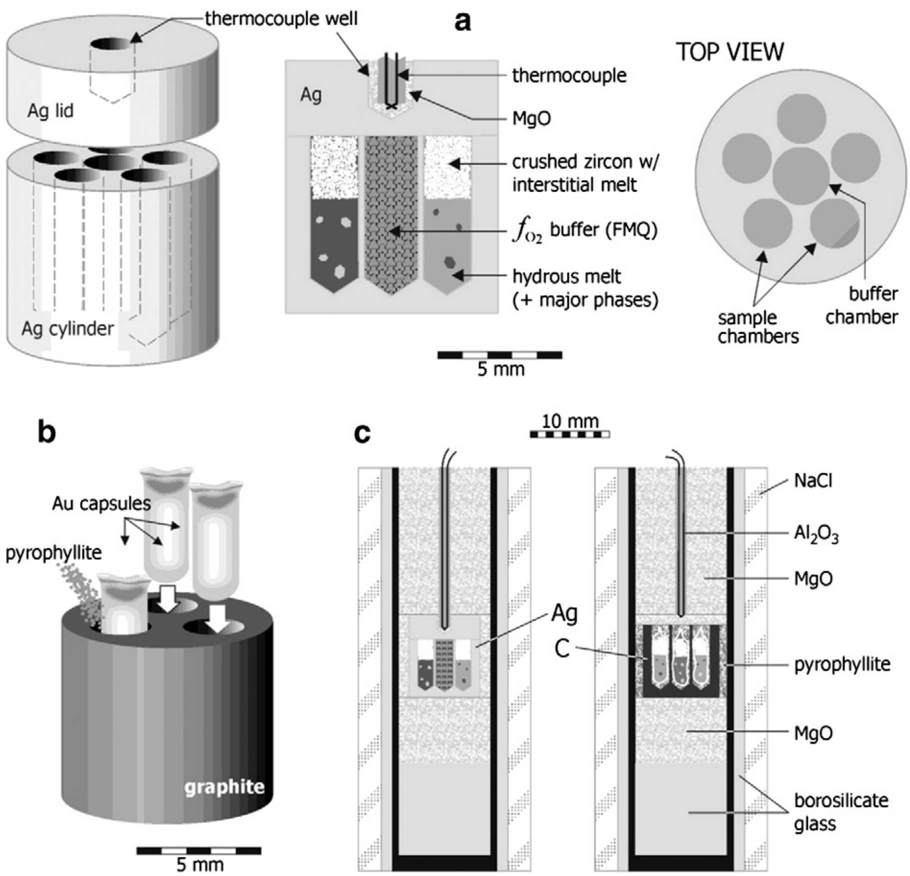

Fig. 2. Schematic illustrations of the two container systems used for the zircon solubility experiments. (a) Three perspectives of the pressure-sealing Ag cylinder with 5 sample wells and a central chamber for the FMQ buffer; (b) graphite cylinder drilled to accept 3 pre-welded Au capsules (the void space is filled with pyrophyllite powder); (c) sections through the 19-mm piston-cylinder assembly used for each container system. Scale bars are on the figures; see text for further explanation.

crushed zircon and the synthetic rock powder present in the lower part of the chamber. The idea behind this strategy was that the melt fraction of the starting rock mix would wick into the crushed zircon at run conditions, leaving other silicate phases mainly in the lower portion of the chamber. The intent was that melt penetrating the crushed zircon would attain saturation equilibrium with its host, and form intergranular pools among the zircon grains large enough to analyze for major elements by electron microprobe (EPMA) and for Zr by SIMS. In early experiments, the crushed zircon used in the starting material had been pre-sieved to ~44–72 μm diameter, which resulted in generally small melt pools (<10 μm) with occasional pockets large enough to analyze. In later experiments (ZSAT9 and 10), the relatively uniform zircon fragments were replaced with broader size-spectrum material that had been passed through a 150-μm sieve and also pre-mixed with 20–30% of the starting rock powder.

Prior to an experiment, the central buffer chamber (Fig. 2a) was filled with a mixture of FeO and silicic acid. Heating to run conditions and minor oxidation of this material produces a solid oxygen buffer assemblage of fayalite + magnetite + quartz (FMQ). The H_2O liberated from the silicic acid enables communication, via hydrogen diffusion, between the buffer and the five chambers in the Ag cylinder containing the hydrous zircon-saturation experiments. Previous experiments conducted in the RPI experimental lab suggest that the 'ambient' f_{O_2} of the piston-cylinder assembly (Fig. 2c) at run conditions is not far displaced from the FMQ buffer. The post-experiment presence of all three phases of the buffer assemblage (and H_2O) was confirmed in all cases by optical microscopy and testing with a magnet for the presence of Fe_3O_4. Other studies in the RPI lab using multi-chambered containers have confirmed that the external buffer regulates f_{O_2} in the experimental charges (e.g., Trail et al., 2012). Hydrogen diffuses relatively slowly in Ag relative to Pt and Pd, but the Ag "septa" between the buffer and the experimental charges was thin (200–300 μm; See Fig. 2a), and the temperatures of the experiments were close to the melting point of silver, where hydrogen diffusion is expected to be fast for this metal (Chou, 1986). When the chambers of the silver container were loaded as desired, it was covered with a pressure-sealing Ag lid and positioned in a 19-mm NaCl-borosilicate glass piston-cylinder assembly (Fig. 2c) for treatment at elevated P–T conditions.

A different container system was needed for the highest-temperature experiments (ZSAT11) because 1020 °C is above the melting point of Ag, even at 1 GPa. For ZSAT11, the samples were contained in Au tubes loaded with rock mix and zircon in a manner similar to that used for the lower-temperature experiments. Only three Au capsules could be run at one time (as opposed to five in the silver container system); the most silicic and the most mafic of the compositions listed in Table 1 were omitted from this series. The Au tubes were welded shut and inserted in pre-drilled holes in a graphite cylinder (Fig. 2b). The void space resulting from the somewhat irregular shape of the Au capsules was filled with unfired pyrophyllite powder in order to establish a finite P_{H2O} outside the Au capsules and counteract any tendency for hydrogen loss from the charges at run conditions. This strategy appears to have been successful, because the H_2O contents of the quenched glasses show no evidence of H_2O loss as inferred from the significant difference between analyzed totals and 100 wt.%. Among the new experiments reported here, ZSAT11 was the only one not buffered at FMQ; it is also the only run incorporating a containment system similar to that used in the experiments of Watson and Harrison (1983).

The mafic-system experiments (ZSAT12 and 13) were run nominally dry in graphite capsules (no added H_2O; powders held at 120 °C prior to loading the experiments) at 1 GPa and 1175 and 1225 °C, respectively.

Following treatment at elevated P–T conditions, the samples were quenched by shutting off the power to the furnace, which resulted in cooling to ~200 °C in ~20 s. The generally cylindrical samples were recovered from the piston-cylinder assembly, sectioned roughly along the cylinder axes, and polished (ultimately with colloidal silica) for EPMA and SIMS analysis.

3.1. Electron microprobe analysis

Major element contents of quenched glasses were determined with the RPI CAMECA SX100 electron microprobe. Glass pools free of inclusions were targeted with a 15 kV accelerating potential, a defocused beam of 30 to 40 μm, and a current of 7 to 10 nA. Elements were standardized against synthetic glass standards and silicates. Sodium, Mg, and Si Kα X-rays were collected through TAP crystals. Potassium, P, Ca, and Ti Kα X-rays were collected through large PET crystals and Fe Kα X-rays were measured through a large LIF crystal.

Major element contents and ZrO_2 of ZSAT 12 and 13 where analyzed using the UCLA JEOL JXA-8200 SuperProbe. Glass pools away from other phases were analyzed with a 15 kV accelerating potential, a defocused beam of 8 μm on ZSAT 13 and 2 μm on ZSAT 12, and a current of 15 nA. The 8 μm beam was sufficiently large to prevent Na loss, however some Na may have been lost using the 2 μm beam size.

3.2. SIMS analytical details

A requirement of the dissolution-type experiment is that Zr released from the crushed Mud Tank zircon equilibrates with the melt (Fig. 3) occupying the inter-crystalline vein network. We chose to use the ion microprobe in scanning ion image analysis mode (e.g., Harrison and Schmitt, 2007) to take advantage of the 2D concentration distribution representations which directly permit the assessment of the degree of equilibration within the glass vein networks. In addition to our new dissolution experiments, 22 of the crystallization experiments from the study of Watson and Harrison (1983) were also analyzed.

Epoxy mounts containing the run products were ultrasonically cleaned in a sequence of soapy water, deionized water, and methanol, and then Au coated. Isotope ratios were measured by focusing $^{90}Zr^{+}$ and $^{30}Si^{+}$ sequentially in the axial ETP electron multiplier through the use of peak switching. A mass resolving power (MRP) of ~4000 was sufficient to separate the peaks of interest from molecular interferences without the use of energy filtering. For these analyses, we used a primary beam of ~50 pA O^{-} in critical illumination with an ~3 μm diameter spot for the July 2007 and August 2011 analyses and an ~8 pA O^{-} and ~4 μm spot for the February 2012 measurements rastered at 20 kHz over a 30 × 30 μm^2 area. For the May 2012 session a primary beam of ~50 pA O^{-} with an ~3 μm diameter spot was used. A dynamic transfer deflection synchronized the primary beam raster with secondary ion beam deflection such that the secondary beam was constantly aligned with the center of the field aperture. Although ion yields vary greatly across the rastered field due to differential charging (which increases with distance from the edge of the analysis area), this effect can be compensated for by ratioing $^{90}Zr^{+}$ to $^{30}Si^{+}$, which is homogeneously distributed throughout the glass. Integration times were ~25 min over 100 cycles (1 cycle = 15 s).

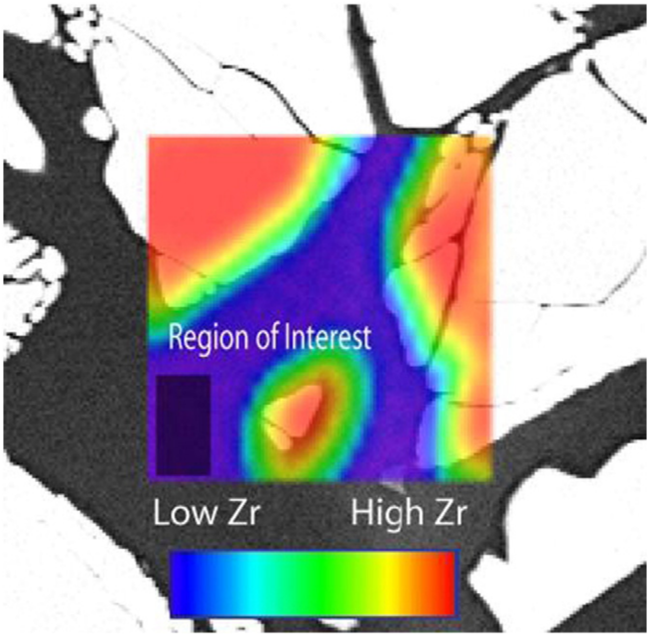

Fig. 3. Scanning ion image of a run product from this study superimposed on the BSE image. The bright regions are the crushed Mud Tank zircon and the ROI for the saturation measurement is shaded ([Zr] = 1000 ppm). Note the absence of neoformed zircon.

All analytical sessions used LCO-1 hydrous glass as the primary standard to determine relative sensitivity factors for Zr/Si, but we also included SRM 610 (and 612) glasses as secondary standards. We rationalize that using LCO-1 as a primary standard mitigates variations in SIMS Zr/Si relative sensitivities (i.e., matrix effects) that are expected for different bulk compositions (e.g., experimental glasses vs. SRM 610). We did not employ energy filtering in an attempt to mitigate matrix effects due to the generally low count rates. In the course of our study, we determined that Zr/Si relative sensitivities increase with the addition of water (all other components being equal). We subsequently (during the August 2011 session) evaluated matrix effects across the range of experimental glass compositions (i.e., between felsic LCO-1 and mafic AGV-1 glasses). Two additional standards were adopted for the February 2012 session to assess the functional form of the correction which appears broadly linear. The overall magnitude of the felsic-to-mafic matrix effect (i.e., the change in $^{90}Zr^{+}/^{30}Si^{+}$ between felsic and mafic standards) depends on the specific run conditions (presputter time, presputter beam current, etc.) and was ~10% and ~20% in the August 2011 and February 2012 sessions, respectively. The sign of this change also depends on specific run conditions and varied between positive and negative in the two sessions, the cause for this being a strong dependence of the relative sensitivity on secondary ion energy due to localized charging of the analysis area. The May 2012 data was corrected using the same correction scheme as for the previous runs. The July 2007 data was corrected using the August 2011 correction scheme as they were collected under similar run conditions.

In contrast to the crystallization experiments (Fig. 1), note in Fig. 3 that the analysis region of interest is free of neoformed zircon seeds. For quantitative imaging of the unknowns, we subdivided the image area into nine equal-size squares to provide an estimate of homogeneity in the standards and examined a region of interest (ROI) sufficiently removed from zircon to avoid beam overlap (Fig. 1).

3.3. Error estimation

There are two dominant sources of uncertainty: elemental abundance and/or ratio precision (assessed via counting statistics) and matrix effects. Overall errors were obtained by adding in quadrature the error calculated from counting statistics with the error from the slopes of the matrix effect calibration lines. Uncertainty due to actual sample heterogeneity is not considered because of the averaging nature of the ion imaging method. The 2σ uncertainties in the ratio varied between 2 and 24% while uncertainties in the calibrations added another 2 to 6% depending on the magnitude of the correction.

4. Results

The complete data set (Table 3) was first plotted with respect to *M* and [Zr] (Fig. 4) to allow comparison with the Watson and Harrison (1983) data. The data at 1020 ºC and 925/950 °C clearly array in a

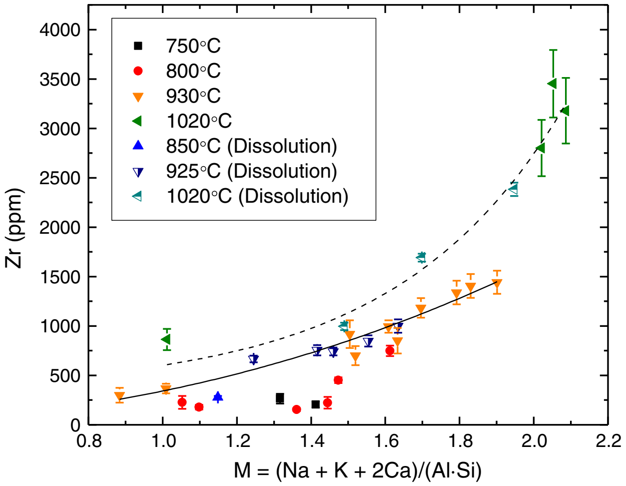

Fig. 4. [Zr] measured on the SIMS plotted versus M. The two lines are fits to the data at 930 °C and 1020 °C (solid and dashed lines respectively). There is good resolution at high temperatures (>900 °C) becoming less so at lower (<900 °C) temperatures. The errors bars are at the level of 2σ.

systematic fashion while the <900 °C data show greater scatter. Our new results (Fig. 4) are remarkably similar to that presented in Fig. 1 of Watson and Harrison (1983). The biggest difference comes from the improved precision of the SIMS measurements as well as the confirmation that $[Zr]_{sat}$ was reached since 1) element gradients were not seen in the 2D ion images, and 2) both the crystallization and dissolution experiments define the same relationship (Fig. 4).

A plot of $\ln(D_{Zr})$ vs. $10^4/T(K)$ as a function of M (Fig. 5) shows more clearly that even the lower temperature data (<900 °C) contain valuable solubility information. The near parallel nature of these lines is evidence that the formulation of compositional dependence of Watson and Harrison (1983) appropriately describes the dataset. Part of scatter in the lines may reflect the effect of compositional interpolation (i.e., there is a range of ±0.1 in M for each line).

4.1. EPMA vs. SIMS

Results from quantitative ion imaging of the crystallization experiments were compared to the EPMA data of Watson and Harrison (1983) in Fig. 6. A least squares regression with a slope of 1.03 ± 0.05 and MSWD of 0.84 was calculated using the New York Regression (Mahon, 1996). Since the slope is indistinguishable from unity, we rule out any significant systematic difference between the EPMA and SIMS data sets.

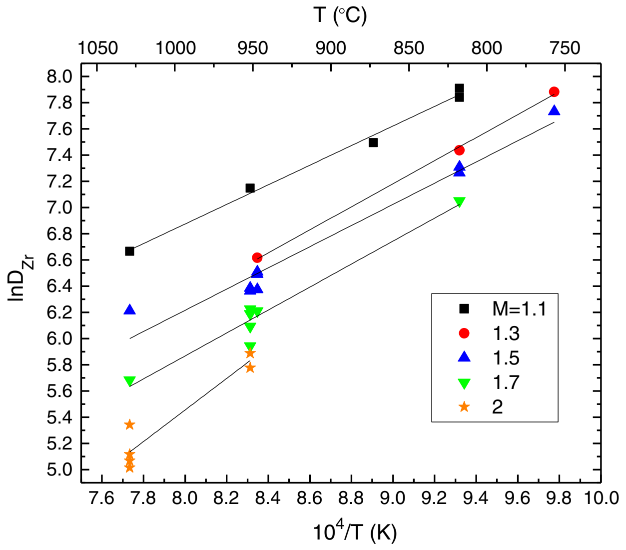

Fig. 5. All SIMS data (this study) plotted on a graph of $\ln(D_{Zr})$ versus inverse absolute temperature. The lines are linear fits (for a constant M); their quasi-parallel nature suggests that the functional form of the model is generally valid.

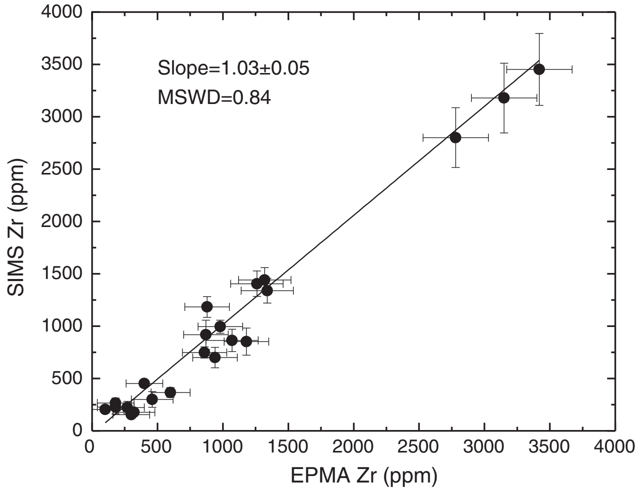

Fig. 6. EPMA data (Watson and Harrison, 1983) plotted against SIMS data (this study). The best fit line has a slope indistinguishable from unity, ruling out any systematic biases between the two data sets. The error bars are at the level of 2σ.

4.2. Model calculation approach and fit

Our view is that it is inadvisable to directly combine the present SIMS dataset with the EPMA data of Watson and Harrison (1983) to calculate a new model as they were obtained under very different analytical conditions. However, the use of both is highly desirable as it prevents over-fitting a refined model by any one data set. The fact that the $\ln(D_{Zr})$ vs. $10^4/T(K)$ plot (Fig. 5) for constant M shows broadly parallel lines implies that the Watson and Harrison (1983) model is broadly consistent with our new results. Rather, our focus is to optimize model parameters about the original formulation while assessing the possibility of a pressure effect.

The original model of Watson and Harrison (1983) was obtained largely by visual curve fits to the [Zr] vs. M data. In our updated model, we utilized the Bayesian Linear Regression (BLR) method which allows for the calculation of a set of parameters based on the data from a prior probability distribution for the parameters (Gelman et al., 2003). First, a BLR was calculated for the Watson and Harrison (1983) data with an uninformative prior distribution (a uniform distribution from negative to positive infinity for each parameter). To produce the final model, a BLR was then calculated using the SIMS data and the output from the first BLR as the prior distribution. This has the effect of allowing the SIMS data to 'update' the model parameters.

In order to determine which parameters (i.e., P, T, and M) are most important to the fit, several models were calculated, each considering a different subset of the parameters. Calculations were performed using MCMCpack (http://mcmcpack.wustl.edu/) and the R statistical software package (http://www.r-project.org/). Bayes Factors were calculated for each regression model in order to identify the best model (Kass and Raftery, 1995). To simplify the selection process, each Bayes Factor was converted into a probability — assuming that one of the models is correct. Model probabilities were calculated from Bayes Factors as their probabilities are normalized, unlike, say, using marginal log likelihoods (Gelman et al., 2003). Note that Bayesian methods calculate the *evidence* for a hypothesis rather than just the probability that a hypothesis is consistent with the given data (such as a T-test). Furthermore, when evaluating models of differing complexity, the goodness of fit is potentially misleading as it biases towards the selection of the most

Table 4
Probabilities for each of the calculated models. Assumed in calculating these probabilities is that one of the models is correct (i.e., probabilities sum to unity).

Model	Probability
T	7.7×10^{-6}
M	0.0021
P	2.67×10^{-12}
$T + P$	0.0002
$P + M$	1.79×10^{-7}
$T + M$	0.9975
$T + M + P$	0.0002

complex parameterization. When selecting among models, the principle of parsimony requires that complexity be penalized.

Given that P was explicitly included in the model calculation, we performed an omnibus fit on the entire dataset including the reanalyzed samples from Rubatto and Hermann (2007). Surprisingly, the probability of the $T + M$ model is 0.9975 with all other permutations yielding coefficients less than 0.002 (Table 4). Thus the best fit model (with 1 σ errors) is given by

$$\ln D_{\mathrm{Zr}} = \frac{10108 \pm 32}{T(K)} - (1.16 \pm 0.15)\cdot(M-1) - (1.48 \pm 0.09). \qquad (2)$$

Discussions of pressure, H_2O, fO_2, etc. effects follow, but note that the above model is specifically formulated to address peraluminous and metaluminous, rather than peralkaline (Watson, 1979) compositions.

5. Discussion

5.1. New parameters

The model parameters in Eq. (2) are broadly similar to those of Watson and Harrison (1983) with differences arising from the improved analytical and computational methods. Comparison of the original and new models (with a nominal 5% error in T) for a constant M of 1.4 shows generally similar temperatures (Fig. 7A). Although the models diverge as M increases (for a constant $[\mathrm{Zr}]_{\mathrm{sat}} = 150$ ppm; Fig. 7B), differences are not significant at the level of uncertainty specified.

In order to estimate the uncertainty of calculated model temperatures, we used standard error propagation techniques to derive the following two formulas:

$$\sigma_{\mathrm{Zr}} = \frac{\sigma_{\mathrm{Zr_{ppm}}}}{\mathrm{Zr_{ppm}}}\cdot D_{\mathrm{Zr}} \qquad (3)$$

$$\sigma_T = \left(\frac{\left(\frac{\sigma_{\mathrm{Zr}}}{D_{\mathrm{Zr}}}\right) + 1.3456\cdot\sigma_{\mathrm{M}}^2}{\ln(D_{\mathrm{Zr}}) + 0.32 + 1.16\cdot M}\right)\cdot T \qquad (4)$$

where σ_{Zr} and σ_T are the one standard deviations of the Zr distribution coefficient and calculated temperature, respectively. The quantities $\mathrm{Zr_{ppm}}$, M, σ_{M}, and σ_{Zrppm} are thus obtained from sample analysis, D_{Zr} is defined in Eq. (1) and T is calculated from Eq. (2).

5.2. Compositional parameterization

The original justification for M was to capture the likely zircon solubility dependence on the product of (Na + K + 2Ca)/Al (i.e., the ratio of network modifiers to formers) and inverse silica activity (Watson and Harrison, 1983). That 1/Si appears to capture this latter control (rather than using $1/a_{\mathrm{Si}}$) was judged more valuable than the fact that M is not dimensionless (it has units atom^{-1}) and thus requires compositional re-normalization. Specifically, our method for calculation of M requires the transformation of the wt.% oxides listed in Table 3 to atomic proportions, re-normalization to total moles, and then the insertion of the Na, K, Ca, Al, and Si molar fractions (over the total number of moles) into the M formulation.

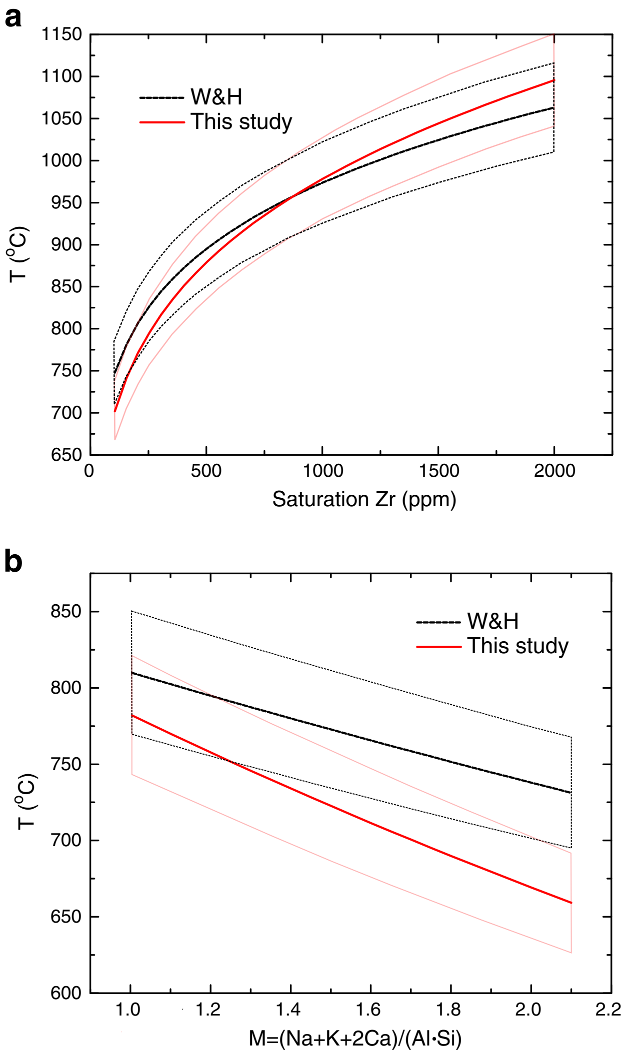

Fig. 7. Plotted in A are both models for a constant M (=1.4). Plotted in B are both models for a constant $[\mathrm{Zr}]_{\mathrm{sat}}$ (=150 ppm). Error envelope representing 5% uncertainty are shown for both lines.

We have examined several ways to modify M as to be dimensionless without success. For example, instead of Al·Si in the denominator, using Al + Si might capture the necessary compositional dependence while removing the dimensional character of M. However, we found that doing so increases the average difference between the calculated and known temperatures for the calibration data by a factor of two. Another approach might be to explicitly use $1/a_{\mathrm{Si}}$. We investigated this approach by calculating silica activities for the 930 °C melt compositions using MELTS (Ghiorso and Sack, 1995; Asimow and Ghiorso, 1998) but found that the correlation coefficient between the saturation concentration and M decreased from 0.95 to 0.7.

A second inconvenience of M arising from its dimensional character is the need to renormalize molar abundances of all major element oxides. Calculating M using molar abundances of only the elements of which it is comprised, nearly identical temperatures (within 10 °C) and similarly high correlation coefficients of 0.99 for the solubility model are obtained as for the original approach of calculating M in Watson and Harrison (1983). Thus, while the calculation of M is inconvenient (and because of the normalization indirectly dependent on other, typically minor components in evolved melts such as Fe and Mg), given the 30 year investment in this approach and significant literature available for comparison, we do not think this issue is significant enough to warrant a change in approach.

Baker et al. (2002) suggested that *FM* (=(Na + K + 2(Ca + Mg + Fe)/(Al·Si)); Ryerson and Watson, 1987) might be a better choice of compositional parameter than *M*. We repeated the procedure described earlier to assess whether *M* or *FM* best represents the compositional controls on zircon solubility for the compositional range. We found that replacing *M* with *FM* in our model results in a substantial deterioration of fit (i.e., $p = 0.19$ vs. $p = 0.81$) and thus conclude that *M* is a far preferable compositional proxy.

5.3. Effect of f_{O_2} and halogens

Baker et al. (2002) measured the diffusion of Zr and zircon solubility in hydrous, metaluminous granitic melts with and without halogens (Cl or F) at 1050–1400 °C and 10 kbar. Their results indicated an 800 °C solubility about one third of that predicted by the Watson and Harrison (1983) model which they attributed to differences in f_{O_2} affecting the structural role of iron in the melt. However, the Baker et al. (2002) data plot (Fig. 8) is reasonably close to our new model fit strongly suggesting that the earlier perceived differences were due to weak control of the model across much of the temperature range used by Baker et al. (2002). Furthermore, this general agreement suggests little influence of oxygen fugacity on zircon solubility and a minimal role of iron and halogens at the levels used by Baker et al. (2002).

5.4. Pressure effect

Rubatto and Hermann (2007) measured $[Zr]_{sat}$ in granitic ($M \approx 1.1$) melts at 20 kbar and reported [Zr] ~40–70% lower than that predicted by Watson and Harrison (1983). Given this disparity, we investigated the possible role of pressure by both undertaking higher pressure dissolution experiments and re-analyzing the run products from the experiments of Rubatto and Hermann (2007), graciously provided by the authors. We undertook two hydrothermal runs at 25 kbar and 930° and 1000 °C, with each run containing five capsules bearing melts of differing composition ($1.3 \leq M \leq 1.5$). Measurement of these glasses (Fig. 9) yield estimates of $[Zr]_{sat}$ that are not significantly different from the predictions of either the model of Watson and Harrison (1983) or this study.

As for the Rubatto and Hermann (2007) glasses, when we standardized using SRM 610 without the matrix corrections (discussed in the SIMS analytical details section) we found remarkable agreement with the concentrations they report. However, given that their glasses were reported to contain ~12% H_2O, when we applied the hydrous and composition matrix corrections, Zr concentrations increased to levels consistent with Watson and Harrison (1983) and this study. We cannot be sure what the full explanation is for this disparity but speculate that it could reflect a matrix mismatch between SRM 612 and the experimental glasses under LA-ICPMS analysis. For example, evidence for this kind of matrix effect has been reported by Gaboardi and Humayun (2009).

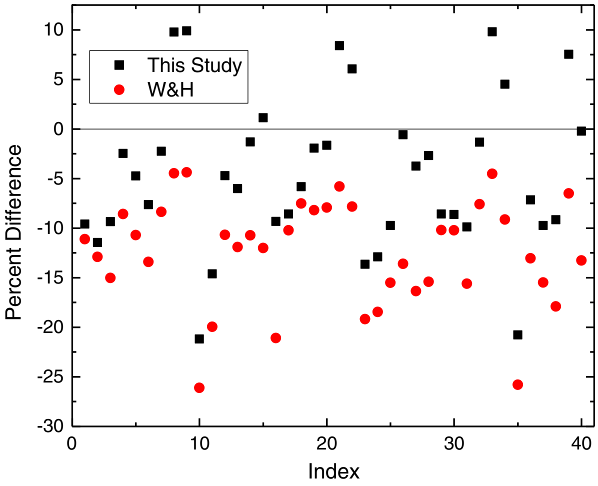

Fig. 8. Results from Baker et al. (2002) compared with model predictions for both the Watson and Harrison (1983) model and this study. The systematic offset in the prediction from the Watson and Harrison (1983) model is eliminated in this study due to a more accurate parametrization.

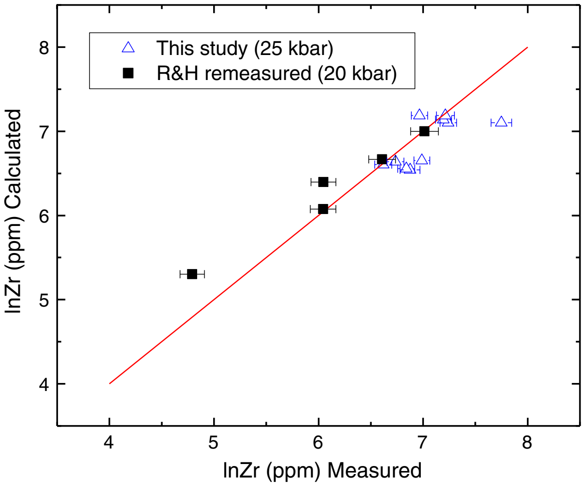

Fig. 9. Dissolution experiments and samples from Rubatto and Hermann (2007) (measured May 2012) plotted with the calculated values. There is no observable pressure effect at 20–25 kbar.

5.5. Implication for melt structure

Previous work on silicate melt structures as a function of pressure suggested that Al^{3+} may shift from four-fold coordination to six-fold coordination at ~15 kbar (Kushiro, 1976). If correct, then it seems likely that the further melt depolymerization at higher pressure would result in an increase in zircon solubility. Allwardt et al. (2005) showed that the coordination change depends on melt composition and that Ca has a large influence in lowering the required pressure from >30 kbar to <20 kbar. However, our experimental samples contained Ca and yet we find that zircon saturation is independent of pressure at or below 25 kbar. Although our experiments were not designed to be a sensitive test of this hypothesis, our results are consistent with little change in Al coordination at ≤25 kbar.

5.6. Effect of water

Given the significant influence of water on Zr diffusion coefficient below ~2% H_2O (Harrison and Watson, 1983), it seems likely that water content could have an effect on zircon solubility. In order to evaluate this possible effect, we compiled the anhydrous data of Harrison and Watson (1983), Ellison and Hess (1986) and Dickinson and Hess (1982) on a plot of $\log(D_{Zr})$ versus inverse absolute temperature and compared it to predictions of our new model (Fig. 10). For *M* corresponding to the lunar granitoid composition of Dickinson and Hess (1982) (i.e., 1.79), the new model does a poorer job than the original of predicting Zr concentration, but the opposite is true for the fit to the Ellison and Hess (1986) and Harrison and Watson (1983) data. Thus the core issue in this apparent reversal of behavior is unlikely to be the presence or absence of water. It is far more likely that this disagreement reflects the lunar compositions of Dickinson and Hess (1982) which lie outside the terrestrial compositional range used in the new calibration together with its high accuracy. The wide range of H_2O concentrations used in the present study and that of Baker et al.

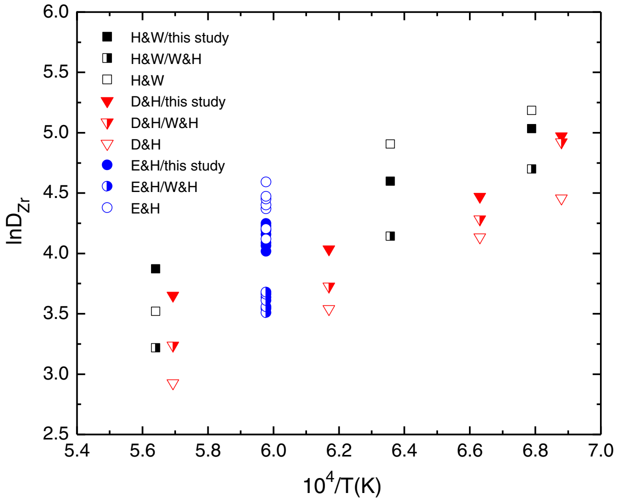

Fig. 10. Results from Harrison and Watson (1983), Ellison and Hess (1986) and Dickinson and Hess (1982) are plotted with predictions for each data set calculated with the Watson and Harrison (1983) model as well as this study. For each study the data is presented in the unfilled symbol, the Watson and Harrison (1983) model in the half filled symbol, and this study in the filled symbol. The Harrison and Watson (1983) study is represented by black squares, the Ellison and Hess (1986) study in blue circles and the Dickinson and Hess (1982) study in red upside down triangles.

(2002) which are both well fit by our preferred model parameters suggests that water content does not strongly influence zircon solubility.

5.7. Zircons from mafic melts?

Zircon is not uncommon in mid-oceanic ridge (MOR) environments (Coogan and Hinton, 2006; Grimes et al., 2007; Fu et al., 2008; Lissenberg et al., 2009; Schmitt et al., 2011), which might be seen to suggest that it can crystallize from basaltic melts close to the liquidus. Although the model we present is not specifically calibrated for such compositional (i.e., $M > 2.5$) or temperature (>1100 °C) conditions, extrapolation suggests zircon could not crystallize from a MORB source above ~900 °C assuming any realistic Zr content. DeLong and Chatelain (1990) found systematic relationships for evolved MOR glasses on plots of M vs. [Zr] using the Watson and Harrison (1983) calibration. At high values of M (3.5 to 2.5), Zr concentrations rise from ~100 to ~700 ppm (at $M = 2.4$) due to the fractionation of modal phases, whereupon [Zr] rapidly decreases with decreasing M. They interpreted this concentration reversal to indicate that zircon began crystallizing at ~840 °C. While $M = 2.4$ is above the highest value of 2.1 used in both the Watson and Harrison experiments and the present study, this small extrapolation seems warranted as the DeLong and Chatelain (1990) 840 °C estimate corresponds well to the solidus temperature of MORB gabbro under water-saturated conditions (Coogan et al., 2001; Botcharnikov et al., 2008). Furthermore, this prediction is consistent with a large database of Ti thermometry for MOR at 800 ± 100 °C (e.g., Grimes et al., 2007; Hellebrand et al., 2007; Fu et al., 2008; Grimes et al., 2008, 2009; Lissenberg et al., 2009; Schmitt et al., 2011; cf. Coogan and Hinton, 2006).

To directly test this proposed relationship, we undertook several experiments (Table 5) using tonalitic to basaltic compositions in order to establish the solubility of Zr in mafic magmas. Analysis of four different compositions at 1225 °C and three at 1175 °C yield ZrO_2 contents between 0.5 and 4.8 wt.% (Table 5). All run products contained neoformed zircons (in addition to plagioclase and pyroxene for ZSAT 12) and each temperature cohort yield a positive correlation between ZrO_2 and M. These results show conclusively that basaltic liquids require an unrealistically high abundance of >5000 ppm Zr to directly crystallize zircon, and thus zircons found in mafic environments must have crystallized from late stage, evolved melts.

Fu et al. (2005, 2008) appear to hold a further misapprehension regarding zircon crystallization from mafic magmas. They viewed the low Ti contents (8–10 ppm) in zircons from anorthosite and gabbroic rocks with liquidus temperatures of ~1000–1100 °C as inconsistent with primary zircon crystallization. However, the low [Zr] of these magmas (ave. = 64 ppm, n = 69; Seifert et al., 2010) effectively precludes stabilizing igneous zircon, even during the fractionation of Zr-poor modal phases (Harrison et al., 2007), until temperatures of ≤750 °C are reached.

5.8. Geologic controls

Because of the relatively poorer resolution of the empirical model at lower temperatures, we compared our model with natural examples from volcanic systems where glass compositions and temperatures are known from other thermometers. There are abundant literature examples where the Watson and Harrison (1983) zircon thermometer has been successfully applied to volcanic rocks (e.g., Hanchar and Watson, 2003), but vagaries exist in how input parameters for the model have been acquired and implemented (including the use of whole-rock vs. glass compositions, or the determination of Zr abundances being biased by method or laboratory). We thus focus on the example of the rhyolitic Bishop Tuff because 1) it has been intensely studied with a wealth of data for various magmatic thermometers being now available, and 2) we have compositional data acquired in-house under similar conditions as in this study, thus minimizing the potential for analytical bias. For our comparison, we use the UCLA CAMECA *ims*1270 data from Schmitt and Simon (2004) to determine Zr abundances in melt inclusion glasses from Bishop Tuff. Here, we only consider data for the F6 unit of the early erupted Bishop Tuff (EBT) which has more homogeneous crystal populations and shows less evidence for strong pre-eruptive re-heating and compositional mixing compared to the late erupted Bishop Tuff (e.g., Wark et al., 2007; Thomas et al. 2010; Reid et al., 2011). Zr abundances were corrected for the hydrous vs. anhydrous matrix effect (i.e., Zr values increase by 20% relative to those in Table 2 of Schmitt and Simon, 2004). With the old calibration (Watson and Harrison, 1983), the average Zr-saturation temperature for the melt inclusions (n = 10) is 745 °C (minimum 729 °C; maximum 758 °C), whereas the new calibration yields an average of 704 °C (minimum 682 °C; maximum 730 °C). This new value compares favorably with Fe–Ti-oxide results – a rapidly equilibrating thermometer closely tracking the eruption temperature – with most data for the EBT ranging between 700 °C and 720 °C (Ghiorso and Evans, 2008).

Table 5
Experimental results including run duration (hours), T (°C), P (kbar), major oxide composition of the melt (wt.%), and ZrO_2 (wt.%).

Sample	Duration	T	P	Analytical total	SiO_2	TiO_2	Al_2O_3	FeO	MgO	CaO	Na_2O	K_2O	ZrO_2	M
ZSAT12B	43.1	1175	10	98.6	62.0	0.1	15.6	7.1	2.4	4.9	3.1	2.7	0.5	1.84
ZSAT12D	43.1	1175	10	98.2	54.0	1.8	16.2	8.8	4.1	6.5	4.0	1.9	1.0	2.43
ZSAT13A	48	1225	10	98.9	47.1	1.5	15.3	8.9	8.1	10.1	2.8	0.2	4.8	3.35
ZSAT13B	48	1225	10	99.4	58.8	0.1	17.5	5.7	2.7	5.9	3.8	1.9	3.0	1.95
ZSAT13C	48	1225	10	99.4	52.4	1.0	18.4	5.2	4.2	9.6	3.6	0.5	4.5	2.61
ZSAT13D	48	1225	10	99.5	53.5	1.1	17.2	6.7	5.1	6.5	3.8	1.2	4.4	2.21

5.9. Implications for lower crustal heat production

A longstanding view among many geochemists is that abundances of certain LILE and HFSE elements decrease with depth in the continental crust (e.g., Rudnick and Gao, 2003). This has generally been assumed to be due to intracrustal magmatic differentiation in which incompatible elements, including U, Th and K and thus heat generation, are partitioned into granitic melts which then buoyantly ascend to the upper crust (e.g., Taylor and McLennan, 1985; Kempton et al., 1995). However, Harrison et al. (1986) noted that because U and Th are largely hosted in the continental crust in accessory phases which remain largely unmelted and unentrained during anatexis, the removal of minimum melts from the lower crust would actually increase uranogenic and thorogenic heat generation there. Our refined model remains consistent with this conclusion for zircon-hosted U and Th, which is further bolstered by the observation of exceedingly low transport rates of U and Th in zircon (Cherniak and Watson, 2003) under crustal conditions, essentially precluding diffusive equilibration during melting. Furthermore, recent models of the composition of the continental crust (e.g., Hacker et al., 2011) emphasize that existing geochemical and geophysical constraints are consistent with considerably greater heat production in the lower crust than previously thought.

6. Conclusions

We revisited the experimental calibration of zircon solubility in crustal melts using improved experimental, analytical and computational approaches. Our new SIMS data reveal no significant difference with that found in the study of Watson and Harrison (1983). Both data sets were used to calculate the parameters for a refined solubility model. The parameters that were found to control zircon saturation behavior are temperature and composition (as represented by *M*). The new model is given by: $\ln D_{Zr} = (10108 \pm 32)/T(K) - (1.16 \pm 0.15)(M - 1) - (1.48 \pm 0.09)$. This refined model predicts broadly similar temperatures for most melt compositions and temperatures as that of Watson and Harrison (1983) but diverges at high zircon concentrations and *M*. There appears to be no pressure effect at ≤ 25 kbar and the compositional parameter *M* is shown to be a superior compositional proxy to a variety of other approaches investigated.

Supplementary data to this article can be found online at http://dx.doi.org/10.1016/j.chemgeo.2013.05.028.

Acknowledgments

We acknowledge Chelsea M. Reed for assistance with the ion image processing, and Drs. Daniela Rubatto and Jörg Hermann (Australian National University) for graciously providing their experimental samples. Helpful comments by journal reviewer Rick Ryerson are acknowledged. This work was supported by the NSF grant EAR-0948724. We acknowledge facility support from the Instrumentation and Facilities Program of the National Science Foundation.

References

Asimow, P.D., Ghiorso, M.S., 1998. Algorithmic modifications extending MELTS to calculate subsolidus phase relations. American Mineralogist 83, 1127–1132.

Allwardt, J.R., Stebbins, J.F., Schmidt, B.C., Frost, D.J., Withers, A.C., Hirschmann, M.M., 2005. Aluminum coordination and the densification of high-pressure aluminosilicate glasses. American Mineralogist 90 (7), 1218–1222. http://dx.doi.org/10.2138/am.2005.1836.

Baker, D.R., Conte, A., Freda, C., Ottolini, L., 2002. The effect of halogens on Zr diffusion and zircon dissolution in hydrous metaluminous granitic melts. Contributions to Mineralogy and Petrology 142, 666–678.

Botcharnikov, R.E., Almeev, R.R., Koepke, J., Holtz, F., 2008. Phase relations and liquid lines of descent in hydrous ferrobasalt — implications for the Skaergaard intrusion and Columbia River flood basalts. Journal of Petrology 49, 1687–1727.

Cherniak, D.J., Watson, E.B., 2003. Diffusion in zircon. Reviews in Mineralogy and Geochemistry 53, 113–143.

Chou, I.M., 1986. Permeability of precious metals to hydrogen at 2 kb total pressure and elevated temperatures. American Journal of Science 286, 638–658.

Coogan, L.A., Hinton, R.W., 2006. Do the trace element compositions of detrital zircons require Hadean continental crust? Geology 34, 633–636.

Coogan, L.A., Wilson, R.N., Gillis, K.M., MacLeod, C.J., 2001. Near-solidus evolution of oceanic gabbros: insights from amphibole geochemistry. Geochimica et Cosmochimica Acta 65, 4339–4357.

DeLong, S.E., Chatelain, C., 1990. Trace-element constraints on accessory-phase saturation in evolved MORB magma. Earth and Planetary Science Letters 101, 206–215.

Dickinson, J.E., Hess, P.C., 1982. Zircon saturation in lunar basalts and granites. Earth and Planetary Science Letters 57, 336–344.

Ellison, A.J., Hess, P.C., 1986. Solution behavior of +4 cations in high silica melts: petrologic and geochemical implications. Contributions to Mineralogy and Petrology 94, 343–351.

Fourcade, S., Allegre, C.J., 1981. Trace elements behavior in granite genesis: a case study. The calc-alkaline plutonic association from the Querigut complex (Pyrenees, France). Contributions to Mineralogy and Petrology 76, 177–195.

Fu, B., Cavosie, A.J., Clechenko, C.C., Fournelle, J., Kita, N.T., Lackey, J.S., Page, F., Wilde, S.A., Valley, J.W., 2005. Ti-in-zircon thermometer: preliminary results. EOS Transactions, pp. V41F–1538.

Fu, B., Page, F.Z., Cavosie, A.J., Fournelle, J., Kita, N.T., Lackey, J.S., Wilde, S.A., Valley, J.W., 2008. Ti-in-zircon thermometry: applications and limitations. Contributions to Mineralogy and Petrology 156, 197–215.

Gaboardi, M., Humayun, M., 2009. Elemental fractionation during LA-ICP-MS analysis of silicate glasses: implications for matrix-independent standardization. Journal of Analytical Atomic Spectrometry 24, 1188.

Gelman, A., Carlin, J.B., Stern, H.S., Rubin, D.B., 2003. Bayesian Data Analysis, Second ed. CRC Press.

Ghiorso, M.S., Evans, B.W., 2008. Thermodynamics of rhombohedral oxide solid solutions and a revision of the Fe–Ti two-oxide geothermometer and oxygen-barometer. American Journal of Science 308, 957–1039.

Ghiorso, M.S., Sack, R.O., 1995. Chemical mass transfer in magmatic processes IV. A revised and internally consistent thermodynamic model for the interpolation and extrapolation of liquid–solid equilibria in magmatic systems at elevated temperatures and pressures. Contributions to Mineralogy and Petrology 119, 197–212.

Grimes, C.B., John, B.E., Kelemen, P.B., Mazdab, F.K., Wooden, J.L., Cheadle, M.J., Hanghøj, K., Schwartz, J.J., 2007. Trace element chemistry of zircons from oceanic crust: a method for distinguishing detrital zircon provenance. Geology 35, 643.

Grimes, C.B., John, B.E., Cheadle, M.J., Wooden, J.L., 2008. Protracted construction of gabbroic crust at a slow spreading ridge: constraints from 206Pb/238U zircon ages from Atlantis Massif and IODP Hole U1309D (30°N, MAR). Geochemistry, Geophysics, Geosystems 9.

Grimes, C.B., John, B.E., Cheadle, M.J., Mazdab, F.K., Wooden, J.L., Swapp, S., Schwartz, J.J., 2009. On the occurrence, trace element geochemistry, and crystallization history of zircon from in situ ocean lithosphere. Contributions to Mineralogy and Petrology 158, 757–783.

Gromet, L.P., Silver, L.T., 1983. Rare earth element distributions among minerals in a granodiorite and their petrogenetic implications. Geochimica et Cosmochimica Acta 47, 925–939.

Hacker, B.R., Kelemen, P.B., Behn, M.D., 2011. Differentiation of the continental crust by relamination. Earth and Planetary Science Letters 307, 501–516.

Harrison, T.M., Schmitt, A.K., 2007. High sensitivity mapping of Ti distributions in Hadean zircons. Earth and Planetary Science Letters 261, 9–19.

Harrison, T.M., Watson, E.B., 1983. Kinetics of zircon dissolution and zirconium diffusion in granitic melts of variable water content. Contributions to Mineralogy and Petrology 84, 66–72.

Harrison, T.M., Watson, E.B., 1984. The behavior of apatite during crustal anatexis: equilibrium and kinetic considerations. Geochimica et Cosmochimica Acta 48, 1467–1477.

Harrison, T.M., Watson, E.B., Rapp, R.P., 1986. Does anatexis deplete the lower crust in heat producing elements?: implications from experimental studies. Transaction of the American Geophysical Union (EOS), 67, p. 386.

Harrison, T.M., Watson, E.B., Aikman, A.B., 2007. Temperature spectra of zircon crystallization in plutonic rocks. Geology 35, 635.

Hanchar, J.M., Watson, E.B., 2003. Zircon saturation thermometry. Reviews in Mineralogy and Geochemistry 53 (1), 89–112. http://dx.doi.org/10.2113/0530089.

Hellebrand, E., Möller, A., Whitehouse, M., Cannat, M., 2007. Formation of oceanic zircons. Goldschmidt Conference Abstracts, p. A391.

Kass, R.E., Raftery, A.E., 1995. Bayes factors. Journal of the American Statistical Association 114, 773–795 (Retrieved from http://www.jstor.org/stable/10.2307/2291091).

Kempton, P.D., Downes, H., Sharkov, E.V., Vetrin, V.R., Ionov, D.A., Carswell, D.A., Beard, A., 1995. Petrology and geochemistry of xenoliths from the Northern Baltic shield: evidence for partial melting and metasomatism in the lower crust beneath an Archaean terrane. Lithos 36, 157–184.

Keppler, H., 1993. Influence of fluorine on the enrichment of high field strength trace elements in granitic rocks. Contributions to Mineralogy and Petrology 114, 479–488.

Kushiro, I., 1976. Changes in viscosity and Structure of melt of NaAlSi2O6 composition at high pressures. Journal of Geophysical Research 81 (35), 6347–6350.

Lissenberg, C.J., Rioux, M., Shimizu, N., Bowring, S.A., Mével, C., 2009. Zircon dating of oceanic crustal accretion. Science 323, 1048–1050.

Mahon, K.I., 1996. The new "York" regression: application of an improved statistical method to geochemistry. International Geology Review 38, 293–303.

Rapp, R.P., Watson, E.B., 1985. Solubility and Dissolution Behavior of Monazite and LREE Diffusion in a Hydrous Granitic Melt. EOS, p. 416.

Reid, M.R., Vazquez, J.A., Schmitt, A.K., 2011. Zircon-scale insights into the history of a Supervolcano, Bishop Tuff, Long Valley, California, with implications for the Ti-in-zircon geothermometer. Contributions to Mineralogy and Petrology 161 (2), 293–311. http://dx.doi.org/10.1007/s00410-010-0532-0.

Rubatto, D., Hermann, J., 2007. Experimental zircon/melt and zircon/garnet trace element partitioning and implications for the geochronology of crustal rocks. Chemical Geology 241, 38–61.

Rudnick, R.L., Gao, S., 2003. Composition of the continental crust. Treatise on Geochemistry 3, 1–64.

Ryerson, F.J., Watson, E.B., 1987. Rutile saturation in magmas: implications for Ti–Nb–Ta depletion in island-arc basalts. Earth and Planetary Science Letters 86, 225–239.

Schmitt, A.K., Simon, J.I., 2004. Boron isotopic variations in hydrous rhyolitic melts: a case study from Long Valley. California. Contributions to Mineralogy and Petrology 146 (5), 590–605. http://dx.doi.org/10.1007/s00410-003-0514-6.

Schmitt, A.K., Perfit, M.R., Rubin, K.H., Stockli, D.F., Smith, M.C., Cotsonika, L.A., Zellmer, G.F., Ridley, W.I., Lovera, O.M., 2011. Rapid cooling rates at an active mid-ocean ridge from zircon thermochronology. Earth and Planetary Science Letters 302, 349–358.

Seifert, K.E., Dymek, R.F., Whitney, P.R., Haskin, L.A., 2010. Geochemistry of massif anorthosite and associated rocks, Adirondack Mountains, New York. Geosphere 6, 855–899.

Taylor, S.R., McLennan, S.M., 1985. The Continental Crust: Its Composition and Evolution. Blackwell.

Thomas, J.B., Watson, E.B., Spear, F.S., Shemella, P.T., Nayak, S.K., Lanzirotti, A., 2010. TitaniQ under pressure: the effect of pressure and temperature on the solubility of Ti in quartz. Contributions to Mineralogy and Petrology 160 (5), 743–759. http://dx.doi.org/10.1007/s00410-010-0505-3.

Trail, D., Watson, E.B., Tailby, N.D., 2012. Ce and Eu anomalies in zircon as proxies for the oxidation state of magmas. Geochimica et Cosmochimica Acta 97, 70–87.

Wark, D.A., Hildreth, W., Spear, F.S., Cherniak, D.J., Watson, E.B., 2007. Pre-eruption recharge of the Bishop magma system. Geology 35 (3), 235.

Watson, E.B., 1979. Zircon saturation in felsic liquids: experimental results and applications to trace element geochemistry. Contributions to Mineralogy and Petrology 70, 407–419.

Watson, E.B., Harrison, T.M., 1983. Zircon saturation revisited: temperature and composition effects in a variety of crustal magma types. Earth and Planetary Science Letters 64, 295–304.

Watson, E.B., Harrison, T.M., 1984a. Accessory minerals and the geochemical evolution of crustal magmatic systems: a summary and prospectus of experimental approaches. Physics of the Earth and Planetary Interiors 35, 19–30.

Watson, E.B., Harrison, T.M., 1984b. What can accessory minerals tell us about felsic magma evolution? A framework for experimental study. Proceedings of the 27th International Geological Congress, pp. 503–520.